npj | flexible electronics

Article

Published in partnership with Nanjing Tech University

https://doi.org/10.1038/s41528-024-00347-7

Interplay between strain and charge in $Cu(In,Ga)Se_2$ flexible photovoltaics

Ha Kyung Park[1,5], Kanghoon Yim[2,5], Jiyoon Lee[1], Yunae Cho[3], Inyoung Jeong[3], Donghyeop Shin[3], Jihye Gwak[3], Aron Walsh[1,4], Kihwan Kim[3] ✉ & William Jo[1] ✉

Flexible and lightweight $Cu(In,Ga)Se_2$ (CIGS) thin-film solar cells are promising for versatile applications, but there is limited understanding of stress-induced changes. In this study, the charge carrier generation and trapping behavior under mechanical stress was investigated using flexible CIGS thin-film solar cells with various alkali treatments. Surface current at the CIGS surface decreased by convex bending, which occurs less with the incorporation of alkali metals. The formation energy of the carrier generating defects increased in convex bending environments clarifying the degradation of the surface current. Moreover, alkali-related defects had lower formation energy than the intrinsic acceptors, mitigating current degradation in mechanical stress condition. The altered defect energy levels were attributed to the deformation of the crystal structure under bending states. This study provides insights into the mitigating of strain-induced charge degradation for enhancing the performance and robustness of flexible CIGS photovoltaic devices.

The recent expansion of the solar energy market has amplified the crucial role of flexible and lightweight thin-film solar cells in reducing manufacturing cost and broadening photovoltaic applications. Among the light-absorbing materials, $Cu(In,Ga)Se_2$ (CIGS) is a promising candidate for commercialized flexible thin-film solar cells due to its high efficiency and stability. Especially, the highest efficiency of 23.6% for CIGS thin-film solar cells was recently reported by Keller et al., achieved through high concentration alloying of Ag[1].

Conventionally, the record cells have achieved a high efficiency of over 22% with alkali fluoride (AlkF) post-deposition treatments (PDT), especially when Rb and Cs are used[2–4]. The incorporation of heavy-alkali (Rb, and Cs) PDT in addition to light-alkali (Na) has a synergistic effect to maximize the device performance increasing the carrier concentration and improving the grain growth[5]. Furthermore, the PDT of alkali elements boosts the performance of flexible CIGS solar cells with a substrate that does not contain alkali elements[6–8]. Notably, flexible CIGS solar cells with a polyimide (PI) substrate exhibited the efficiency of 20.82% when the doping of heavy-alkali (RbF) PDT was controlled[9]. Recently, Ishizuka et al. reported flexible minimodules with an efficiency of 18.6% by Rb-PDT and also an efficiency of 18.5% by Na- and K-PDT[10].

For flexible solar cells, understanding the characteristics of CIGS materials under stress is crucial to developing mechanically robust devices. However, changes in the flexible CIGS solar cells under mechanical stress and stress-induced modifications in CIGS materials have not been extensively examined. Few reports on the degradation of device performance after mechanical bending tests are available[11,12]. In light of this, we previously demonstrated that the incorporation of alkali in flexible kesterite solar cells improved the stress-induced loss in the local open-circuit voltage (V_{OC}) by designing a measurement system based on scanning probe microscopy that can be applied to a bent surface[13].

In this study, changes in the electrical charge states of flexible CIGS thin-film solar cells doped with alkali (e.g., Na, Rb and Cs) were investigated under mechanical bending stress. Under mechanical bending, the lattice constants changed, leading to the rearrangement of elements. Herein, based on scanning probe microscopy, the surface current of a bent surface was measured by attaching flexible CIGS samples on metal holders with specific curvatures. The distribution of current on the surface of the flexible CIGS improved with alkali incorporation and was degraded under mechanical bending stress due to alterations in the charged states. However, CIGS with additional alkali incorporation exhibited significantly suppressed degradation even under the bending states. Density functional theory (DFT) study provided insights into the strain effect on CIGS films at the atomic level, potentially revealing the underlying mechanism for the reduced degradation observed in alkali-incorporated CIGS films under bending stress. We conclude that defect-level redistribution with alkali incorporation enhances the tolerance of CIGS thin films to mechanical stress.

[1]Department of Physics, Ewha Womans University, Seoul, 03760, Korea. [2]Computational Science and Engineering Laboratory, Korea Institute of Energy Research, Daejeon, 34129, Korea. [3]Photovoltaics Research Department, Korea Institute of Energy Research, Daejeon, 34129, Korea. [4]Department of Materials, Imperial College London, London, SW7 2AZ, UK. [5]These authors contributed equally: Ha Kyung Park, Kanghoon Yim. ✉e-mail: kimkh@kier.re.kr; wmjo@ewha.ac.kr

Methods

Film/device fabrication

A PI film was used as the flexible substrate with a DC-sputtered Mo coating (700 nm) as a back contact. Three-stage co-evaporation method was used to grow the CIGS thin films with additional in-situ alkali PDT. The nominal thickness of the alkali (Na, Rb, Cs) PDT layer was 10 nm. Additional annealing with Se supply (15 Å/s) was performed after the alkali PDT. The temperature for the whole process was maintained under 450 °C. To complete the device fabrication, 40–60 nm of the CdS buffer layer was deposited on the CIGS thin film by using chemical bath deposition. Then, 50 nm of intrinsic zinc oxide (i-ZnO) and 150 nm of indium tin oxide (ITO) layer were deposited by radio frequency (RF) sputtering. An aluminum (Al) top electrode was deposited, and 110 nm of magnesium fluoride (MgF_2) was deposited for anti-reflect coating by using electron beam evaporation.

Characterization

The *J-V* characteristics of the finished devices were measured with a solar simulator (WACOM, WXS-155S-L2), under a standard test condition of AM 1.5 G spectrum and intensity of 1 sun (100 mW·cm^{-2}) at 25 °C. The temperature-dependent V_{OC} (V_{OC}-T) was performed using a semiconductor characterization system (Keithley 4200, Tektronix, Inc.). A vacuum probe stage with a temperature controller (HFS600E-PB4, Linkam) was used to vary the temperature from 300 K to 80 K with an interval of 10 K at a pressure of 10^{-3} Torr. For the temperature-dependent *C-V*, DLCP, and AS measurements, a LCR meter (Agilent 4284 A) was used with a probe station (LTS 350, Linkam) applying the same temperature interval as the V_{OC}-T measurement. The microstructures and element distribution were characterized by transmission electron microscopy (TEM; JEM-ARM200F "NEO ARM", JEOL) and energy-dispersive X-ray spectrometry (EDS, JED-2300T(Dual), JEOL), respectively. The accelerating voltage for the STEM observations was 200 kV. A cross-section lamella of the CIGS thin film for the TEM measurement was prepared using a focus-ion beam system. An O_2 sputtering source was used for the time-of-flight secondary ion mass spectrometry (ToF-SIMS) measurements instead of the Cs source to avoid the detection of a potential Cs source. For the XRD measurements, the height of the samples loaded were adjusted to be identical to avoid the influence of the difference of the distance between the sample and the detector.

c-AFM measurements

Commercial atomic force microscopy (Nanofocus, n-tracer) was used to perform conductive-atomic force microscopy (c-AFM) measurement. Contact mode was used to scan the surface, and the set point value was 1 nN. A Pt/Ir-coated tip (Nanocensors Inc.) was used for the measurement. An external bias of 0.5 V (DC) was applied to the sample stage with the tip grounded, and the detection limit of the surface current was 10 nA. The scan area was 2 × 2 μm^2, and the scan resolution was 256 × 256 pixels (256-line scan). During the scanning, the scan rate was maintained below 0.3 Hz to minimize the tip damages. Herein, obtaining topography and surface current maps under concave bending with a curvature angle of 30° (corresponding to a curvature radius of 14 mm) proved challenging due to technical issues, specifically the movement of the cantilever was hindered by the curved mold. Strain (ε) applied to the thin film can be calculated by following equation[14]:

$$\varepsilon(\%) = \frac{(r_\theta + t_{substrate} + t_{film})\theta - r_\theta\theta}{r_\theta\theta} \times 100 \quad (1)$$

where θ is a curvature angle and r_θ is a radius of curvature. $t_{substrate}$ and t_{film} are thickness of the substrate and film, respectively. When the curvature angle is 30°, applied strain is approximately 1%. Samples were attached to the mold using a carbon tape. To prevent delamination of the CIGS layer from the PI substrate when detaching the sample from the carbon tape, the center of the sample was adhered to the curvature mold, and the edge of the sample was wrapped with carbon tape. Silver paste was used to create electrical contacts.

DFT calculations

Total energy and electronic structure calculations were performed using density functional theory (DFT). The Vienna Ab initio Simulation Package[15] with projector augmented-wave pseudo-potentials was employed. The generalized gradient approximation was applied for the exchange-correlation function, and the DFT + U method was used for Cu with U_{eff} = 4 eV for the d states[16]. A $CuIn_{0.5}Ga_{0.5}Se_2$ unit cell was used to represent the complex configurational space of CIGS. The energy cut-off of the plane-wave basis was set to 300 eV, and k-points were sampled as 3 × 3 × 2 Monkhorst-pack mesh that satisfy the convergence criteria of energy/atom < 0.01 eV and pressure < 10 kBar. To calculate the defect chemistry at the CIGS GBs, a 148-atom slab structure with (112) surface was used. The initial (112) surface structure was made stoichiometric, but we found that the V_{Cu} at the upper surface voluntarily formed. Therefore, we use the thermodynamically stabilized Cu-poor surface structure in which all Cu sites at the upperrmost surface are vacant. The defect formation energy (E_f) was calculated as follows:

$$E_f(defect) = E_{tot}(defect) - E_{tot}(perfect) + \sum N_i\mu_i + q(\varepsilon_F + \varepsilon_{VBM}) + E_{corr},$$

where E_{tot} is the total free energy of the supercell; and N_i and μ_i are the quantities and chemical potentials of the exchanging chemical species, respectively. For a charged defect, q is the charge state of the defect, ε_F is the Fermi level from the valence band maximum (ε_{VBM}), and E_{corr} is the charge correction energy determined using the Makov-Payne method[17]. To calculate the changes in lattice parameters under biaxial strain, we modify the VASP code to allow the lattice relaxion only along the z-axis. For all calculations, atomic configurations were optimized, until the atomic force converged within 0.01 eV/Å.

Results and discussions

CIGS crystal structure and distribution of alkali elements at the grain boundaries (GBs) were determined from high-resolution scanning transmission electron microscopy (STEM) image, as shown in Fig. 1a. The d-spacing obtained using the fast-Fourier transform (FFT) patterns was 0.329 nm, which corresponded to the CIGS grain with (1 1 2) orientation and assuming (1 1 2) facets facing GBs. The distribution of alkali elements was investigated by STEM-energy dispersive spectroscopy (EDS) measurements. In Fig. 1b, c, the GBs of the heavy-alkali-doped CIGS showed a Cu-depleted composition. By contrast, the concentration of heavy alkali increased at the GBs compared to the intragrain regions, suggesting heavy alkali occupation of the Cu vacancy sites. Several studies have demonstrated empirically and theoretically the segregation of heavy alkalis toward the GBs, in which the heavy alkalis pushed light alkalis away from the GBs[18–20]. The segregation of heavy alkali toward GBs passivated the detrimental defects and modified the energy level of the Cu vacancy (V_{Cu}) sites[21,22]. However, the migration of expelled light alkalis is debating. On the one hand, several studies have indicated that relatively light alkali was pushed away toward the surface. On the other hand, some studies showed that the repelled light alkali accumulated in the grain interior[23–25]. The EDS images of other elements are presented in Supplementary Fig. 1. Herein, the concentration of Na was under the detection limit of EDS, which hindered the identification of the presence of Na.

In addition to the expulsion of the light alkali at the GBs, the in-depth intensity of Na decreased significantly after the heavy-alkali PDT compared to that of the CIGS sample with NaF PDT only. Figure 1d shows that the in-depth distribution of Na was hardly detected in the heavy-alkali PDT CIGS, and this result was comparable to the TEM-EDS results. The significant decrease in Na in the entire film suggested that the light alkalis from the GBs repelled by the heavy alkalis apparently moved toward the surface and washed away during the chemical bath deposition of CdS. The intensity of heavy alkalis was higher than that of Na although the nominal thickness of the alkali PDT was identical. The concentration of alkali elements slightly increased at the back of the CIGS absorber due to the higher ionization probability of alkali metals at the oxidized Mo surface, which acts as an alkali

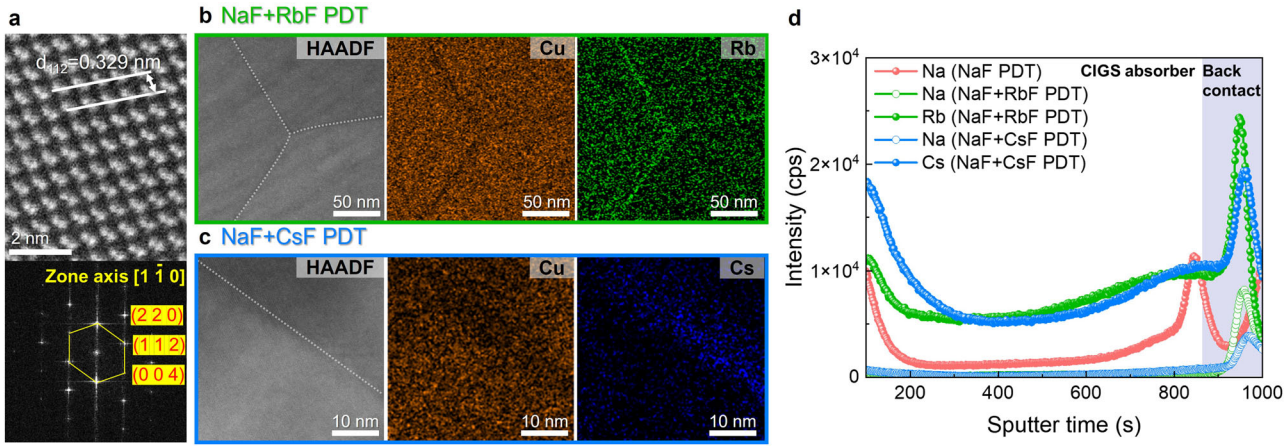

Fig. 1 | Distribution of alkali elements in the bulk and grain boundaries (GBs). **a** High-resolution STEM image of the grain with (1 1 2) orientation. Inset presents the fast-Fourier transform (FFT) image of the white dashed box area in Fig. 1a. **b**, **c** Scanning transmission electron microscopy (STEM)-energy dispersive spectroscopy (EDS) images of (**b**) NaF+RbF PDT and (**c**) NaF+CsF PDT samples. High-angle annular dark field (HAADF) images and EDS maps of Cu, Rb, and Cs at the GBs. White dashed line in the HAADF images indicate the random GBs. **d** The depth profile of alkali elements in the alkali PDT CIGS samples was obtained by time-of-flight secondary ion mass spectrometry (SIMS).

reservoir, while the CIGS/Mo interface is also the GBs of the CIGS[24]. Additionally, a previous study has demonstrated that the concentration of Rb at the GBs increased toward the Mo back contact[5]. None of the alkali elements were detected in the non-PDT CIGS samples by SIMS, as the PI polymer substrate does not contain alkali elements.

To investigate the carrier behavior under mechanical stress, the current at the surface was probed using conductive-atomic force microscopy (c-AFM). As shown in Fig. 2a, a sample holder with curvature mold was prepared to apply artificial concave and convex bending to the flexible CIGS thin-film[13,14]. Mechanical stress was continuously applied as the samples were attached to the holder. Therefore, formation of the surface current during mechanical bending was obtained directly as the bent CIGS absorber surface was probed. Severe cracks or breakage induced by the stress were not observed in the topographies, indicating that the CIGS mechanically tolerated the strain with bending radius of 20.47 mm (See Supplementary Fig. 2). A previous study has also presented that the CIGS thin-film tolerated tensile stress lower than 1.0%, and stress of more than 1.0% resulted in grain boundary (GB) cracking that affected the carrier transportation along the GBs[26].

The surface current flowed along the GB of CIGS thin film, as depicted in the surface current map in Fig. 2b. A two-dimensional (2D) topography and surface current map of all CIGS can be found in Supplementary Fig. 3. This illustration highlights the GBs as the main conduction channels, particularly, when an external bias is applied to the sample emitting electrons from the samples to the grounded tip[27]. The samples with alkali PDT showed enhanced formation of the surface current presumably due to the increased carrier concentrations. Additionally, Sharma et al. recently demonstrated that the CIGS thin film treated with Rb and Cs possessed higher carrier concentrations and enhanced homogeneity of carrier concentration[28]. The segregated alkalis at GBs changed the charged defect states, resulting in different electrostatic properties[29–31].

The quantitative distribution of the surface current from the two-dimensional current maps is shown in Fig. 2c, in which the surface current values from 20 GBs were extracted. The distribution of the surface current significantly decreased under convex bending, indicating a decrease in conductivity. A comparison between samples with and without mechanical stress history is presented in Supplementary Fig. 4. Under convex bending, the surface current decreased in the CIGS samples both with and without alkali PDT. However, CIGS with alkali PDT showed less degradation in surface current compared to the CIGS without PDT, which showed a remarkable decrease in current. Some GBs of the alkali PDT CIGS maintained original values even under convex bending, indicating that the presence of alkali elements at the GBs hindered the decrease in conductivity. The electrical properties at the GBs could be attributed to the distribution of defect states. Therefore, changes in the surface current under mechanical bending might have originated from the redistribution of defect states at the GBs.

To investigate how the changes in defect states at CIGS GBs depend on strain, we conducted DFT calculations to determine the formation energies of various defect states, including intrinsic and alkali-incorporated defects, under varying strain conditions. Assuming that GBs perpendicular to the film surface are relevant to the region where the highest current peak is observed in c-AFM images, we consider the strain conditions in the concave and convex bending states as shown in Fig. 2d. Under concave bending, the compressive axial stress within the film induces planar expansion of grain boundaries (GBs). Conversely, the opposite effect, GB contraction, is expected under convex bending. Given that (1 1 2) facets with copper deficiency are expected to be dominant GBs in CIGS as shown in Fig. 2d, we adopt the Cu-deficient (1 1 2) surface structure obtained from our previous study to effectively mimic the defect chemistry at GBs[20]. Among all calculated defect configurations (see Supplementary Fig. 5 and Supplementary Table 1 for the all considered defects), defect complexes combining alkali interstitials (Na_i, Rb_i, and Cs_i) and Cu vacancy (V_{Cu}) have the lowest defect formation energies. More specifically, larger alkali metals tend to have lower defect formation energies when incorporated next to the V_{Cu} defect. This explains why rubidium (Rb) and cesium (Cs) dominate at grain boundaries (GBs) in NaF+RbF and NaF+CsF PDT CIGS, respectively. These defect complexes (Na_i-V_{Cu}, Rb_i-V_{Cu}, and Cs_i-V_{Cu}) differ from Cu substitutional defects (Na_{Cu}, Rb_{Cu}, and Cs_{Cu}) as alkali metals does not occupy the Cu sites. Notably, Rb_{Cu} and Cs_{Cu} have much larger formation energy compared to Rb_i-V_{Cu}, and Cs_i-V_{Cu} suggesting that Rb and Cs cannot permeate into intragrain. Interestingly, while these defect complexes (Na_i-V_{Cu}, Rb_i-V_{Cu}, Cs_i-V_{Cu},) are electrically neutral, the formation energies of additional V_{Cu} near the Na_i-V_{Cu} complex is even lower than V_{Cu} without PDT. This provides feasible explanation for the origin of the largest current increasement at GBs in NaF PDT CIGS. In Fig. 2e, the calculated formation energies of major carrier-generating defects are compared under axial strains on CIGS (1 1 2) surface, ranging from −2% to +2% of the lattice parameters. Under compressive axial strain applied to the (1 1 2) surface of CIGS, which corresponds to the convex bending condition, the formation energy of V_{Cu}^- defects increases, leading to a decrease in carrier concentration. On the contrary, tensile axial stress boost the formation of V_{Cu}^+. Notably, the formation energies of V_{Cu} near Na_i-V_{Cu} complex (V_{Cu}@Na_i-V_{Cu}) is much lower than V_{Cu} that explains the reason that NaF PDT CIGS shows lowest degradation compared to other conditions. On the other hand, the

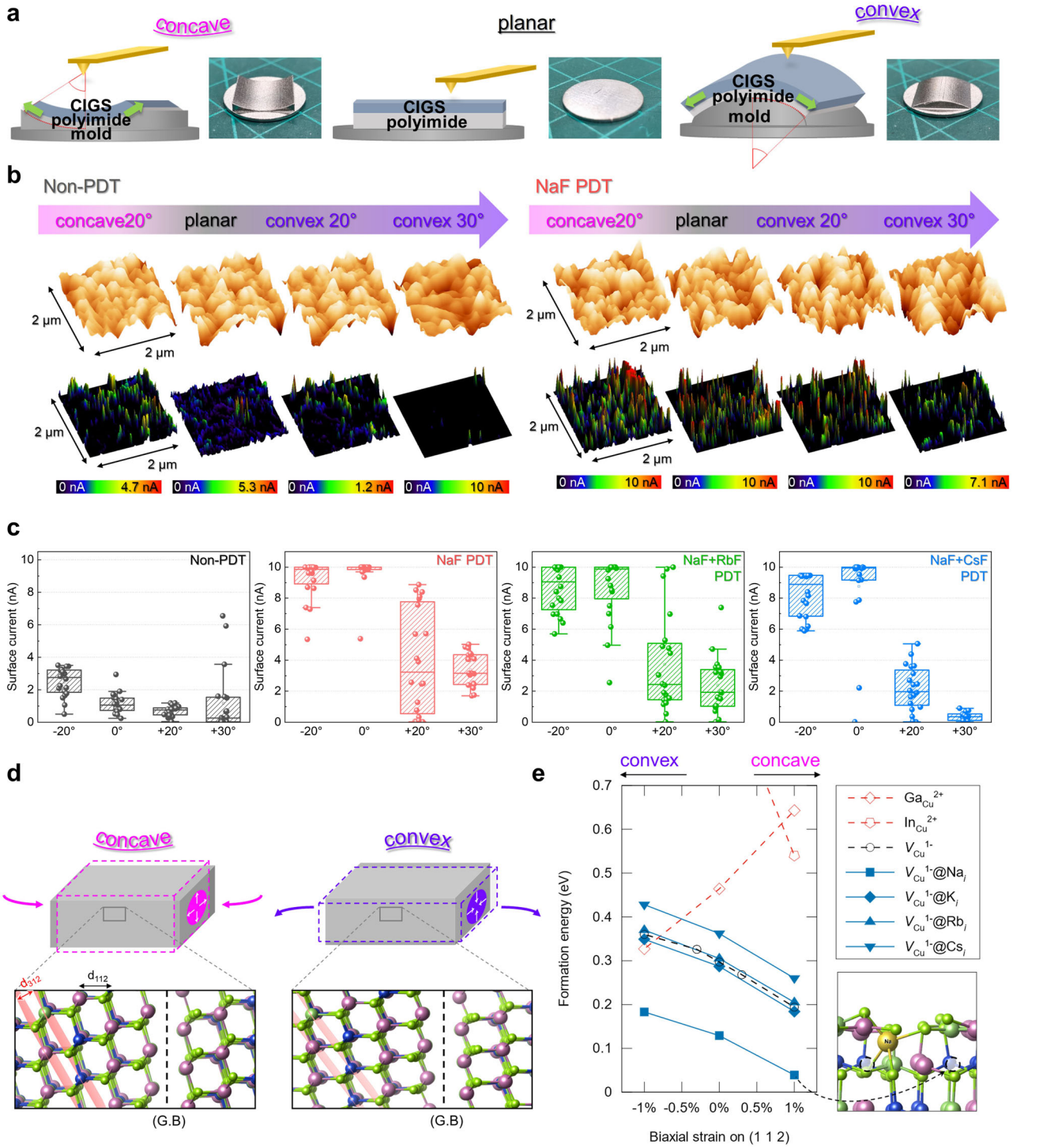

Fig. 2 | Interplay between charge and strain with modification in the defect formation energy under the different bending states. a Schematic diagram of the scanning bent surface by atomic force microscopy and the pictures of the metal mold with specific curvatures. **b** Surface topography and surface current images of the CIGS devices with the concave, planar, and convex bending settings. External bias of 0.5 V was applied to the samples, and the bending radii were 20.47 mm and 14 mm for curvature angles of 20° and 30°, respectively. **c** Box plot of the surface currents extracted from 20 GBs at each sample under planar and mechanical bending states. **d** Schematic illustration of strain relations of concave and convex bending states. Zoomed crystal structure depicts a model atomic structure of CIGS near the GB composed of two (1 1 2) facets under mechanical bending states. **e** Calculated defect formation energies of primary carrier-generating defects, with or without alkali defect complexes, under different biaxial strains.

formation energies of V_{Cu} near K_i-V_{Cu}, Rb_i-V_{Cu}, and Cs_i-V_{Cu} were similar or slightly higher than the V_{Cu} without alkali incorpoaration. Herein, it was assumed that grain boundaries possess a single type of alkali element as heavy alkalis tended to segregate into the GBs by pushing away Na from the GBs as presented in Fig. 1.

To investigate the structural changes in the CIGS with mechanical stress, angle-tilted X-ray diffraction (XRD) measurements were performed for the CIGS both in the planar and bent states. Herein, Ψ indicates the angle between the diffraction scattering vector and the normal direction of samples. In the planar state, the CIGS (3 1 2) orientation peak presented the peak

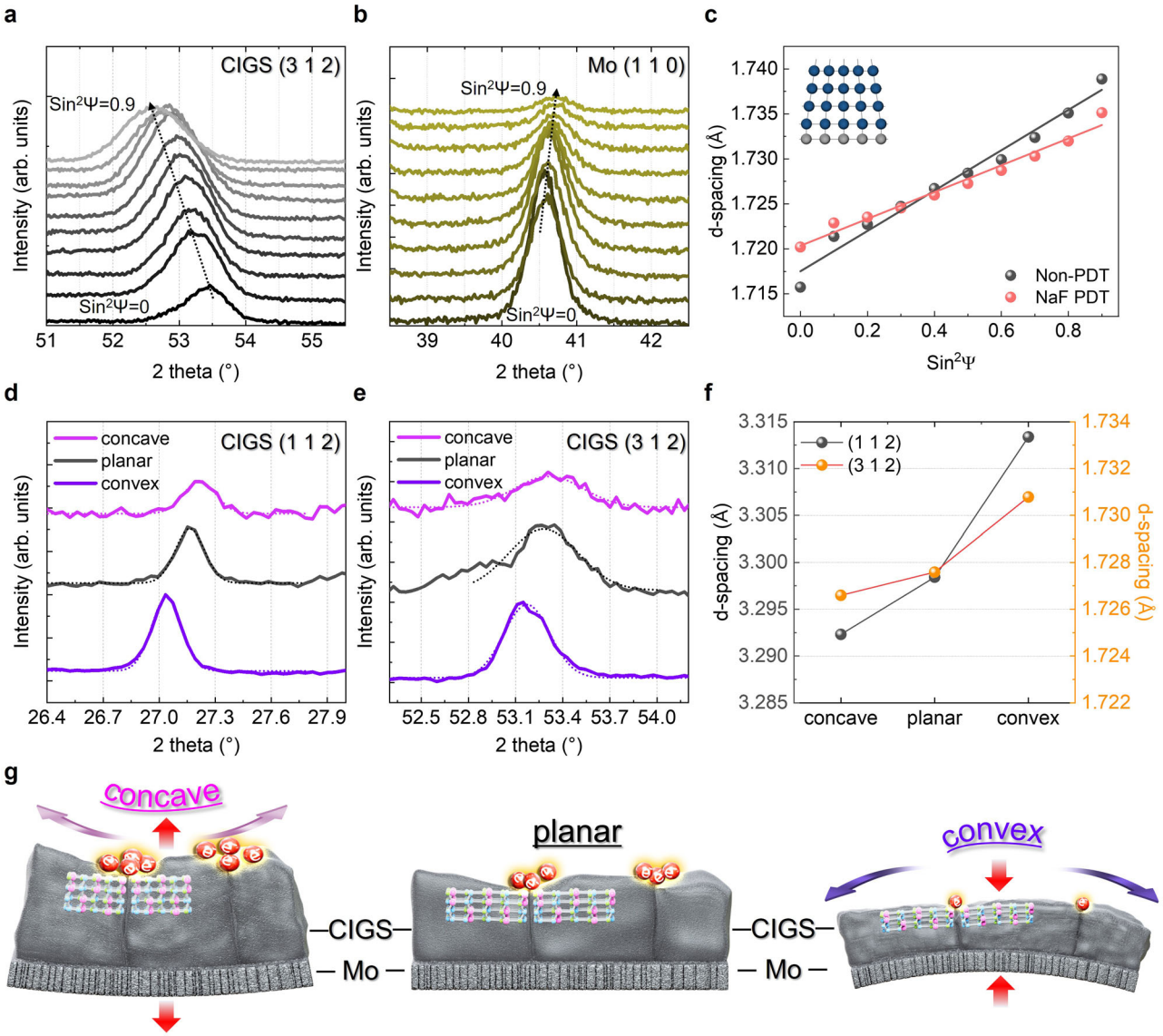

Fig. 3 | Stress analysis of CIGS thin-film in the planar and bending states. **a**, **b** Angle-tilted X-ray diffraction pattern shifting of the (**a**) CIGS (3 1 2) and (**b**) Mo (1 1 0) peaks. By tilting the angle Ψ, the value of $\sin^2\Psi$ value varied from 0 to 0.9 with a step of 0.1. **c** d-spacing change in the (3 1 2) diffraction peak by angle tilting in the Non-PDT and NaF PDT CIGS samples. Inset diagram represents the intrinsic stress in the CIGS thin-film deposited on the Mo back contact layer. **d** CIGS (1 1 2) and (**e**) (3 1 2) orientation peak shift with concave and convex mechanical bending. **f** Quantitative d-spacing change in the CIGS (1 1 2) and (3 1 2) orientation. **g** Schematic diagram of modifications in the GB carrier distribution according to the d-spacing changes under the bending states compared with those of the planar states.

shift toward the lower diffraction angle by tilting angle Ψ, indicating tensile stress. On the other hand, the Mo (1 1 0) peak presented the peak position shift toward a higher angle, indicating compressive stress (Fig. 3a, b). Several previous studies have reported the stress analysis of CIGS thin-films with intrinsic compressive stress when they were deposited on the SLG[32,33]. Tensile stress formed in the CIGS thin film was probably attributed to the relatively thicker Mo back contact layer with smaller thermal expansion coefficient than the CIGS thin film[34].

The angle-tilted XRD patterns of the CIGS samples without PDT and NaF PDT under mechanical bending both presented tensile stress, indicating that mechanical bending did not compensate the intrinsic tensile stress (See Supplementary Figs. 6 and 7). As shown in Fig. 3c, NaF PDT CIGS showed a smaller slope than that of the sample without PDT when the tilting angle was increased, indicating that NaF PDT CIGS had lower residual tensile stress. The NaF PDT CIGS sample presented slightly larger d-spacing compared to that without PDT, because the size of the Na atom was larger than the other elements, thus widening the crystal structure. Therefore, incorporation of the Na atoms produced relative compressive strain through the lattice site by enlarging the d-spacing, thereby slightly compensating the intrinsic tensile stress in the film.

Out-of-plane XRD patterns for the lattice of the thin film were recorded under planar and bent states to measure the crystal plane spacing. The crystal plane spacing perpendicular to the film presents a coherent direction with the crystal structure model of Fig. 2d, with the vertical direction of (1 1 2) facets assumed to be facing GBs. Figure 3d, e demonstrate the shifts of the (1 1 2) and (3 1 2) orientation peaks under mechanical stress. The (1 1 2) and (3 1 2) orientation peaks shifted toward lower diffraction angle (i.e., larger d-spacing) under convex bending, while it shifted toward higher diffraction angle (i.e., smaller d-spacing) under concave bending. These d-spacing changes supported our model for the microdeformation of the crystal structure due to mechanical stress as shown in Fig. 2d. The calculated lattice parameters of CIGS crystal under biaxial strain (see Supplementary Table 2) are also consistent with the XRD analysis.

The correlation between carrier distribution and crystal structure modification is depicted in Fig. 3g. Under convex bending, the biaxial compressive stress in the plane direction led to an increase in the acceptor

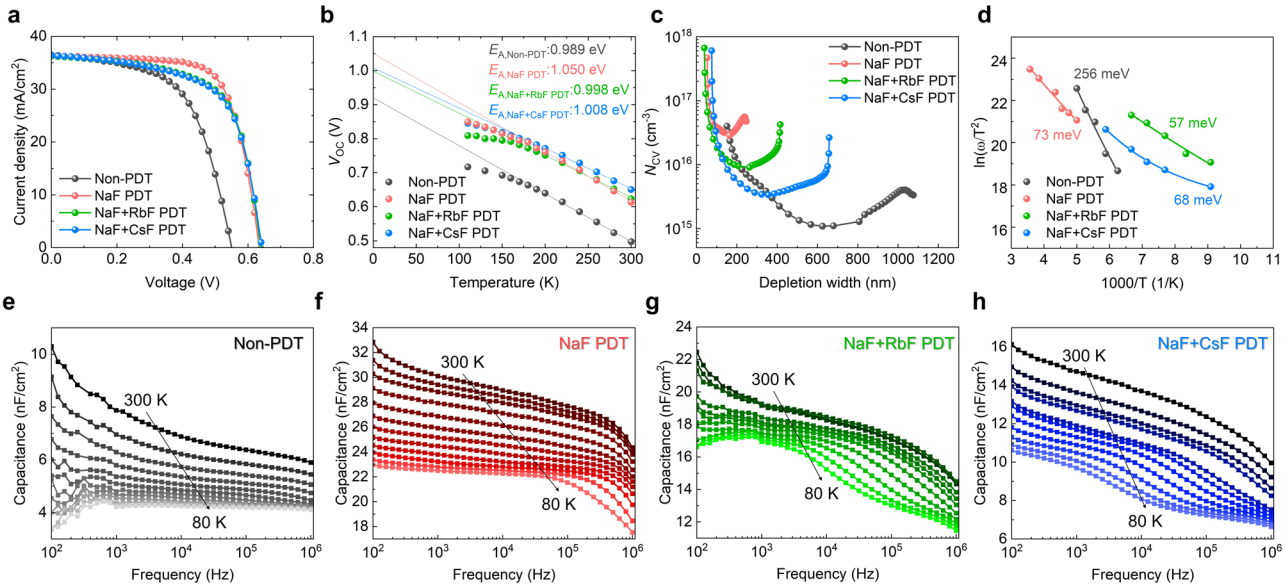

Fig. 4 | Device properties of various alkali-doped flexible CIGS thin-film solar cells. a Current-voltage (*J-V*) curves of four different samples. The NaF+RbF PDT and NaF+CsF PDT samples exhibited comparable curves resulting in an overlap. **b** Temperature-dependent V_{OC} plot for the flexible CIGS thin-film solar cells under illumination. **c** Carrier concentration (N_{CV}) of CIGS thin-film solar cells at 300 K obtained from capacitance-voltage (*C-V*) measurements. **d** Defect energy levels calculated from the Arrhenius plot. **e–h** Admittance spectroscopy of the flexible CIGS thin-film solar cells obtained from 80 K to 300 K.

Table 1 | Photovoltaic device parameters of flexible CIGS solar cell devices with best efficiency in each treatment and N_{CV}

Sample	V_{oc} (V)	J_{sc} (mA/cm²)	FF (%)	PCE (%)	N_{CV} (cm⁻³)
Non-PDT	0.550	37.93	58.0	12.10	1.28×10^{15}
NaF PDT	0.642	36.2	72.8	16.9	2.87×10^{16}
NaF+RbF PDT	0.639	36.29	64.43	14.95	9.05×10^{15}
NaF+CsF PDT	0.642	36.4	63.38	14.81	3.59×10^{15}

energy levels, hindering the generation of charge carriers. By contrast, biaxial tensile stress decreased the energy levels of the acceptor defects under concave bending, thereby maintaining high carrier concentrations. This modification in carrier concentrations according to the mechanical bending can be related to the piezophototronic or flexoelectric effect in a dielectric semiconductor or device[35]. The piezophototronic effect in heterojunction devices facilitates or impedes the transport of photo-generated carriers at the heterojunction interface by mechanical stress modulating the junction region, which in turn affects the photoresponsivity or photovoltaic parameters. The piezophototronic response of the flexible CIGS thin-film optoelectronic devices is increased by the application of artificial static compressive strain, thereby modifying the interface energy band[36,37]. Thus, the enhancement in carrier concentration at the CIGS absorber surface under concave bending can be potentially attributed to the piezophototronic effect in flexible CIGS optoelectronic devices. Additionally, since the CIGS absorber layer is a polycrystalline thin film, the magnitude and distribution of experiencing stress can vary according to the grain size and film thickness. The grain size and thickness of the CIGS thin film are shown in Supplementary Fig. 8.

Figure 4 demonstrated the performances and carrier dynamics of flexible CIGS thin film solar cells. Figure 4a shows the current density-voltage (*J-V*) curve of the flexible CIGS thin-film solar cells, and the photovoltaic parameters are presented in Table 1. CIGS devices with AlkF PDT had enhanced device performances compared to the device without PDT. Among the CIGS samples, the NaF PDT sample exhibited the highest power conversion efficiency, followed by NaF+RbF and NaF+CsF PDT CIGS. The V_{OC} was enhanced with alkali PDT, leading to comparable values among the alkali PDT samples. The alkali PDT samples showed improved fill factor (FF) compared to the samples without PDT, but FF decreased with additional heavy-alkali PDT. The decrease in FF could be attributed to the formation of a thin Alk–In–Se compounds layer that acted as an electron barrier by inducing a downward valence band edge on the low-Ga CIGS surface[23,38,39]. A box plot of the solar cell parameters is presented in Supplementary Fig. 9. Figure 4b presents the temperature-dependent V_{OC} of various alkali-treated CIGS solar cells. Temperature-dependent *J-V* curves for all temperature steps are presented in Supplementary Fig. 10. Activation energy (E_A) could be extracted at the point T = 0 K from the linear fitting of the V_{OC}-T plot when the diode ideality factor was not dependent on temperature[40]. The CIGS devices with AlkF PDT provided the larger E_A compared to the CIGS device without PDT, which exhibited a value of 0.989 eV. Thus, interface recombination was alleviated by AlkF PDT, regardless of the type of alkali used. Among the samples, the NaF PDT samples exhibited the highest E_A value of 1.050 eV.

Carrier concentrations and defect energy levels of various alkali-doped CIGS solar cell were investigated by measuring the capacitance-voltage (*C-V*) characteristics. The results from *C-V* measurements showed that the increase in carrier concentrations (N_{CV}) of samples with alkali PDT samples (Fig. 4c). All alkali PDT samples demonstrated improved N_{CV} compared to the Non-PDT sample, as they enhanced the p-type conductivity. The NaF PDT CIGS had the highest N_{CV}, as it increased the charge carrier density most effectively[41]. In addition, the NaF PDT CIGS sample showed the highest density of free carriers and the lowest density of the deep defects among the alkali PDT samples as presented in Supplementary Fig. 11, Supplementary Tables 3 and 4. The depletion width decreased in alkali PDT samples, which could lead to a reduction in J_{SC} due to hindered photocarrier collection and separation, consistent with previous studies[6,42].

Admittance spectroscopy (AS) measurements were performed to determine the defect energy levels. The energy levels of the defect states as shown in Fig. 4d were calculated using the linear fitting of the Arrhenius plot derived from the derivatives of the AS spectra in Fig. 4e–h. The AS results indicated that irrespective of the type of alkali used, the defect energy levels decreased after alkali treatment compared to the sample without PDT[43]. The alkali PDT samples possessed lower defect energy levels due to the defect passivation effect of the alkali elements[44]. The high density of the defects resulted in the low carrier concentration of the samples without PDT.

By contrast, alkali PDT samples possessed lower trap densities and reduced defect energy levels compared to the samples without PDT. This characteristic could be attributed to higher carrier concentrations as evident in planar state surface current map presented in Fig. 2b. In particular, improved free carrier concentrations with lowered activation energy presumably contribute to lower charge carrier degradation under mechanical bending conditions. Furthermore, the mechanical bending stability of flexible CIGS solar cell devices was evaluated through bending tests. The results showed that device performance did not significantly degrade after 5000 concave and convex bending cycles with a bending radius of 20 mm, which corresponds to the bending radius used in the c-AFM measurements (Supplementary Fig. 12).

In conclusion, the results of the c-AFM measurement performed to probe the surface current of the CIGS thin-film under different mechanical bending states showed that the quantitative surface current was degraded under convex bending. Materials modeling demonstrated that convex bending increased the acceptor defect formation energy, resulting in lower carrier concentrations as observed using the surface current map. Nevertheless, alkali PDT CIGS showed less degradation in the surface current under convex bending, which was attributed to the lower energy level of the alkali-related acceptors. The redistribution of the alkali-related defects was enabled due to the change in crystal plane spacings under the mechanical bending states. These findings suggested that the incorporation of alkali elements improved the stress tolerance in terms of carrier generation. In addition, the mitigation of intrinsic tensile stress in the CIGS thin films deposited on the flexible PI substrates contributed to the reduction in acceptor defect levels and generation of carriers. Thus, the developed probing technique to map the current distribution on a bent surface provides practical information as it simulates the environment experienced by flexible electronic devices in real-world applications.

Data availability

The authors declare that the data supporting the findings of this study are available within the paper and its supplementary information files or available on reasonable request from the authors.

Received: 8 June 2024; Accepted: 3 September 2024;
Published online: 16 September 2024

References

1. Keller, J. et al. High-concentration silver alloying and steep back-contact gallium grading enabling copper indium gallium selenide solar cell with 23.6% efficiency. *Nat. Energy* **9**, 467–478 (2024).
2. Nakamura, M. et al. Cd-Free Cu(In,Ga)(Se,S)2 thin-film solar cell with record efficiency of 23.35. *IEEE J. Photovolt.* **9**, 1863–1867 (2019).
3. Jackson, P. et al. Effects of heavy alkali elements in Cu(In,Ga)Se_2 solar cells with efficiencies up to 22.6. *%. Phys. Status Solidi – Rap. Res. Lett.* **10**, 583–586 (2016).
4. Kato, T., Wu, J.-L., Hirai, Y., Sugimoto, H. & Bermudez, V. Record efficiency for thin-film polycrystalline solar cells up to 22.9% achieved by Cs-treated Cu(In,Ga)$(Se,S)_2$. *IEEE J. Photovolt.* **9**, 325–330 (2019).
5. Raghuwanshi, M. et al. Influence of RbF post deposition treatment on heterojunction and grain boundaries in high efficient (21.1%) Cu(In,Ga)Se_2 solar cells. *Nano Energy* **60**, 103–110 (2019).
6. Kim, K. et al. Mechanisms of extrinsic alkali incorporation in CIGS solar cells on flexible polyimide elucidated by nanoscale and quantitative analyses. *Nano Energy* **67**, 104201 (2020).
7. Chirila, A. et al. Potassium-induced surface modification of Cu(In,Ga)Se_2 thin films for high-efficiency solar cells. *Nat. Mater.* **12**, 1107–1111 (2013).
8. Park, H. K. et al. Tailored band structure of Cu(In,Ga)S_2 thin-film heterojunction solar cells: depth profiling of defects and the work function. *ACS Appl. Mater. Interfaces* **14**, 34697–34705 (2022).
9. Carron, R. et al. Advanced alkali treatments for high-efficiency Cu(In,Ga)Se_2 solar cells on flexible substrates. *Adv. Energy Mater.* **9**, 1900408 (2019).
10. Ishizuka, S., Kamikawa, Y. & Nishinaga, J. Lightweight and flexible Cu(In,Ga)Se_2 solar minimodules: toward 20% photovoltaic efficiency and beyond. *npj Flex. Electron.* **6**, 90 (2022).
11. Tsai, W.-C. et al. Flexible high performance hybrid AZO/Ag-nanowire/AZO sandwich structured transparent conductors for flexible Cu(In,Ga)Se_2 solar cell applications. *J. Mater. Chem. A* **4**, 6980–6988 (2016).
12. Gerthoffer, A. et al. CIGS solar cells on flexible ultra-thin glass substrates: characterization and bending test. *Thin Solid Films* **592**, 99–104 (2015).
13. Park, H. K. et al. Flexible kesterite thin-film solar cells under stress. *npj Flex. Electron.* **6**, 91 (2022).
14. Kim, Y. S., Chung, H., Kwon, S., Kim, J. & Jo, W. Grain boundary passivation via balancing feedback of hole barrier modulation in HfO_{2-x} for nanoscale flexible electronics. *Nano Converg.* **9**, 43 (2022).
15. Kresse, G. & Hafner, J. Ab initio molecular dynamics for liquid metals. *Phys. Rev. B Condens Matter* **47**, 558–561 (1993).
16. Wang, L., Maxisch, T. & Ceder, G. Oxidation energies of transition metal oxides within theGGA+Uframework. *Phys. Rev. B* **73**, 195107 (2006).
17. Makov, G. & Payne, M. C. Periodic boundary conditions in ab initio calculations. *Phys. Rev. B Condens Matter* **51**, 4014–4022 (1995).
18. Schöppe, P. et al. Rubidium segregation at random grain boundaries in Cu(In,Ga)Se_2 absorbers. *Nano Energy* **42**, 307–313 (2017).
19. Chugh, M., Kuhne, T. D. & Mirhosseini, H. Diffusion of alkali metals in polycrystalline $CuInSe_2$ and their role in the passivation of grain boundaries. *ACS Appl. Mater. Interfaces* **11**, 14821–14829 (2019).
20. Kim, K. et al. Atom-scale chemistry in chalcopyrite-based photovoltaic materials visualized by atom probe tomography. *ACS Appl. Mater. Interfaces* **14**, 52825–52837 (2022).
21. Karki, S. et al. Analysis of recombination mechanisms in RbF-treated CIGS solar cells. *IEEE J. Photovolt.* **9**, 313–318 (2019).
22. Lee, H. et al. Passivation of deep-level defects by cesium fluoride post-deposition treatment for improved device performance of Cu(In,Ga)Se_2 solar cells. *ACS Appl. Mater. Interfaces* **11**, 35653–35660 (2019).
23. Helder, T. et al. How small changes make a difference: influence of low silver contents on the effect of RbF-PDT in CIGS solar cells. *Prog. Photovolt. Res. Appl.* **31**, 1205–1214 (2022).
24. Wuerz, R., Hempel, W. & Jackson, P. Diffusion of Rb in polycrystalline Cu(In,Ga)Se_2 layers and effect of Rb on solar cell parameters of Cu(In,Ga)Se_2 thin-film solar cells. *J. Appl. Phys.* **124**, 165305 (2018).
25. Kodalle, T. et al. Elucidating the mechanism of an RbF post deposition treatment in CIGS thin film solar cells. *Sol. RRL* **2**, 1800156 (2018).
26. Yang, C., Song, K., Xu, X., Yao, G. & Wu, Z. Strain dependent effect on power degradation of CIGS thin film solar cell. *Sol. Energy* **195**, 121–128 (2020).
27. Kim, G. Y., Jo, W., Jo, H.-J., Kim, D.-H. & Kang, J.-K. Macroscopic and microscopic electrical properties of Cu(In,Ga)Se_2 thin-film solar cells with various Ga/(In+Ga) contents. *Curr. Appl. Phys.* **15**, S44–S50 (2015).
28. Sharma, D. et al. Charge-carrier-concentration inhomogeneities in alkali-treated Cu(In,Ga)Se_2 revealed by conductive atomic force microscopy tomography. *Nat. Energy* **9**, 163–171 (2024).
29. Siebentritt, S. et al. Heavy Alkali treatment of Cu(In,Ga)Se_2 solar cells: surface versus bulk effects. *Adv. Energy Mater.* **10**, 1903752 (2020).
30. Nicoara, N. et al. Direct evidence for grain boundary passivation in Cu(In,Ga)Se_2 solar cells through alkali-fluoride post-deposition treatments. *Nat. Commun.* **10**, 3980 (2019).
31. Hwang, J. et al. Reforming material chemistry of CIGS solar cells via a precise Ag doping strategy. *J. Mater. Chem. A* **11**, 19546–19555 (2023).

32. Yang, S.-C. et al. Silver-promoted high-performance (Ag,Cu)(In,Ga)Se_2 thin-film solar cells grown at very low temperature. *Sol. RRL* **5**, 2100108 (2021).
33. Mainz, R. et al. Sudden stress relaxation in compound semiconductor thin films triggered by secondary phase segregation. *Phys. Rev. B* **92**, 155310 (2015).
34. Lin, Y.-C. et al. Residual stress in CIGS thin film solar cells on polyimide: simulation and experiments. *J. Mater. Sci.: Mater. Electron.* **25**, 461–465 (2013).
35. Tripathy, A., Saravanakumar, B., Mohanty, S., Nayak, S. K. & Ramadoss, A. Comprehensive review on flexoelectric energy harvesting technology: mechanisms, device configurations, and potential applications. *ACS Appl. Electron. Mater.* **3**, 2898–2924 (2021).
36. Zhu, L. et al. Piezo-phototronic and pyro-phototronic effects to enhance Cu(In, Ga)Se_2 thin film solar cells. *Nano Res.* **11**, 3877–3885 (2018).
37. Qiao, S. et al. Piezophototronic effect enhanced photoresponse of the flexible Cu(In,Ga)Se_2 (CIGS) heterojunction photodetectors. *Adv. Funct. Mater.* **28**, 1707311 (2018).
38. Ishizuka, S., Taguchi, N. & Fons, P. J. Similarities and critical differences in heavy Alkali-metal rubidium and cesium effects on chalcopyrite Cu(In,Ga)Se_2 thin-film solar cells. *J. Phys. Chem. C.* **123**, 17757–17764 (2019).
39. Cheng, S. et al. Analysis of the heavy Alkali element postdeposition treatment: which factors determine the electronic structure and transport properties of the heterojunction in CIGS thin film solar cells. *ACS Appl. Energy Mater.* **4**, 3279–3287 (2021).
40. Cho, Y. et al. Photon-induced defects and dynamics of photogenerated carriers in Cu(In,Ga)Se_2 thin film solar cells. *Sol. Energy Mater. Sol. Cells* **220**, 110860 (2021).
41. Pianezzi, F. et al. Unveiling the effects of post-deposition treatment with different alkaline elements on the electronic properties of CIGS thin film solar cells. *Phys. Chem. Chem. Phys.* **16**, 8843–8851 (2014).
42. Khatri, I., Matsuura, J., Sugiyama, M. & Nakada, T. Effect of heat-bias soaking on cesium fluoride-treated CIGS thin film solar cells. *Prog. Photovolt. Res. Appl.* **27**, 22–29 (2018).
43. Werner, F. et al. Alkali treatments of Cu(In,Ga)Se_2 thin-film absorbers and their impact on transport barriers. *Prog. Photovolt. Res. Appl.* **26**, 911–923 (2018).
44. Colombara, D., Conley, K., Malitckaya, M., Komsa, H.-P. & Puska, M. J. The fox and the hound: in-depth and in-grain Na doping and Ga grading in Cu(In,Ga)Se_2 solar cells. *J. Mater. Chem. A* **8**, 6471–6479 (2020).

Acknowledgements

This research was financially supported by national R&D programs through the National Research Foundation of Korea (grant number: RS-2024-00355905, NRF-2018R1A6A1A03025340, and NRF-2022M3J1A1064229), funded by the Ministry of Education and the Ministry of Science and ICT, and the framework of the Research and Development Program of the Korea Institute of Energy Research (grant number: C4-2412). The first author, H.K.P., gratefully acknowledges the scholarship support received from the Hyundai Motor Chung Mong-Koo Foundation.

Author contributions

H.K.P. and K.Y. contributed equally to this work and the manuscript was mainly written by the first authors. H.K.P. designed the research and performed the T-V_{OC}, DLCP, AS, c-AFM, SEM measurements. K.Y. conceived the computational research and performed the DFT simulations. J.L. contributed to the c-AFM measurement. Y.C. assisted the experiments and characterizations. I.J., D.S. and K.K. designed the fabrication of the flexible CIGS solar cells and conducted the *IV* measurements. J.G. supervised the research program. A.W. contributed the validation of computational study and revised the manuscript. K.K. and W.J. supervised the overall work. All authors discussed the results and commented on the manuscript.

Competing interests

The authors declare no competing interests.

Additional information

Supplementary information The online version contains supplementary material available at https://doi.org/10.1038/s41528-024-00347-7.

Correspondence and requests for materials should be addressed to Kihwan Kim or William Jo.